Undersea Capacitive Coupled Simultaneous Wireless Power and Data Transfer for Multiload Applications

Chaolai Da, Fang Li, Ming Nie, Shufan Li, Chengxuan Tao, *Member, IEEE*, and Lifang Wang, *Member, IEEE*

***Abstract*—This article proposes the implementation of a wireless power supply and data transmission system for automatic underwater vehicle (AUV) clusters in submarine multiload application scenarios, which is based on the principle of single capacitive coupling and comprises a power station at the transmitting side and multiple devices at the receiving side. The power station can charge all devices synchronously while also achieving instructions from the power station to multiple AUVs and the data loading of the power station from each AUV. First, the equivalent circuits of undersea capacitive coupled simultaneous wireless power and data transfer (UCC-SWPDT) system are built and the characterization of the power channel and the bi-directional data channel are investigated. Next, the interference of the power channel to the data channel is analyzed. The modeling of the coupling mechanism in seawater is developed and simulated, while a parametric design procedure for the UCC-SWPDT system is proposed. Finally, a prototype with a total output power of 200 W and a data rate up to 1 Mb/s is built, where the experimental results demonstrate the feasibility of the UCC-SWPDT system proposed in this article to be applied in submerged multiload scenarios.**

***Index Terms*—Multiload wireless power transfer, simultaneous wireless power and data transfer (SWPDT), single capacitive coupling, undersea wireless power transfer (UWPT).**

I. Introduction

UNDERSEA wireless power transfer (WPT) technology has attracted a lot of attention due to its safety and flexibility in recent years, which addresses the wet plug charging of autonomous underwater vehicles (AUV) and the improvement of their endurance [1], [2], [3], [4].

A representative scenario for the application of the WPT technology in seawater is shown in Fig. 1. Photovoltaics, power station, and solid-state battery build a renewable energy system and sensing network, capable of recharging and data interaction with the AUV clusters operating submerged. The captured messages are then uploaded to the mothership on the surface. The key

Received 1 July 2024; revised 13 September 2024; accepted 16 October 2024. Date of publication 21 October 2024; date of current version 12 December 2024. This work was supported by the National Key R&D Program of China under Grant 2021YFC2800200. Recommended for publication by Associate Editor A. Safaee. *(Corresponding author: Fang Li.)*

The authors are with the Key Laboratory of High Density Electromagnetic Power and Systems (Chinese Academy of Sciences), Institute of Electrical Engineering, Chinese Academy of Sciences, Beijing 100190, China, and also with the University of Chinese Academy of Sciences, Beijing 100049, China (e-mail: dachaolai@mail.iee.ac.cn; lifang@mail.iee.ac.cn; nm1999@mail.iee.ac.cn; lishufan@mail.iee.ac.cn; taochengxuan@mail.iee.ac.cn; wlf@mail.iee.ac.cn).

Color versions of one or more figures in this article are available at https://doi.org/10.1109/TPEL.2024.3483956.

Digital Object Identifier 10.1109/TPEL.2024.3483956

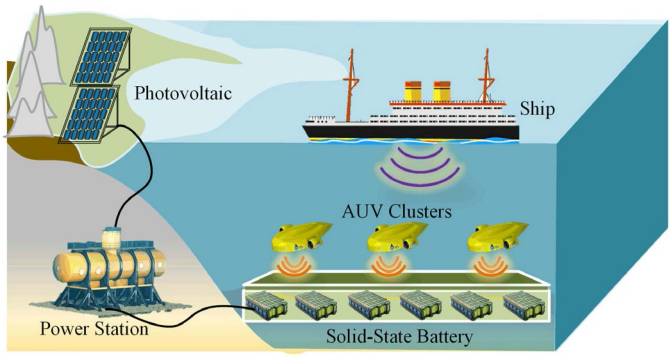

Fig. 1. Schematic of WPT system and sensing network in the submarine.

to this is charging AUV clusters by the power station, a single transmitter and multiple receivers (STMR) WPT technology. The existing research for STMR systems is mainly implemented in air [5], [6], [7], [8].

In [5], [6], and [7], an inductive coupling scheme with coils was employed to implement STMR systems for multiload applications. Nevertheless, the relatively high eddy current losses in seawater over long transmission distances limit the application of this scheme [9], [10]. A double-receiver compact single capacitive coupled WPT (SCC-WPT) system was proposed based on a single capacitance coupled scheme in [8], which has a low number of metal plates and excellent spatial freedom compared to the conventional capacitive coupling WPT system with four metal plates. Although this solution has been implemented and demonstrated to be practical in the air, the influence of seawater on the system characteristics needs to be investigated when this solution is applied to the undersea STMR system.

In addition, the power station sends instructions to the AUV clusters when they are charging. Each AUV needs to upload data to the power station simultaneously [11], [12]. Conventional RF communication schemes degrade dramatically with increasing distance and can only be used for very close transmission distances. In recent research, it has been found that simultaneous wireless power and data transfer (SWPDT) technology is expected to overcome this issue [13], [14], [15], [16]. Several investigations have been carried out in the air [17], [18], [19], [20], [21], providing the basis for SWPDT technology to be applied in seawater.

The research in [17] has shown that it is possible to achieve kW-level power transfer and Mb/s level data rates after optimizing the parameters in the SWPDT system. The SWPDT system

proposed in [18] was capable of achieving full-duplex communication mode with a signal-to-noise ratio (SNR) of 32 dB. In [19], the SWPDT technology was applied to a dynamic wireless charging system for electric vehicles. It is interesting to note that data are transferred through the high-frequency electric field generated by the parasitic capacitances of the coupling coils and the metal shield plates. In addition, in an attempt to investigate the interference of the power channel to the data channel, the suppression of differential mode (DM) interference and common mode (CM) interference in a high-power SWPDT system was proposed in [20]. Based on the above findings, the feasibility of SWPDT technology applied in seawater was also explored and the performance characterization of the system was analyzed in [21], [22], and [23]. However, the present investigations are for single transceiver and single receiver systems, and there is still a research gap for the application of SWPDT technology in STMR systems.

The multiload application scenario shown in Fig. 1 requires not only an STMR WPT system to charge the AUV clusters but also the STMR data channel to accomplish the communications. An SWPDT topology based on STMR systems has been proposed in [6], but it is limited in its application in seawater due to its dependence on the inductive coupling scheme. To extend the transmission distance of the data channel in seawater, the SWPDT systems based on a single capacitive coupled scheme were proposed in [22] and [23]. This is an effective method to achieve simultaneous STMR wireless power and data transfer systems in seawater. Therefore, to implement the requirements of undersea multiload application scenarios, this article proposes an undersea capacitive coupled simultaneous wireless power and data transfer (UCC-SWPDT) system based on the single capacitive coupled principle for multiload applications.

The SCC-WPT system has been implemented in several works [24], [25], [26], [27]. In this article, the application scope of the SCC-WPT system is extended, which can construct multiple power channels and bidirectional data channels in seawater. Also, the UCC-SWPDT system is capable of achieving SWPDT in multiload application scenarios for submarine environments. The contributions of this article are summarized as follows.

1) A topology of single transmitter and multiple receivers system is proposed based on the single capacitive coupling principle in submerged environments. In contrast to the inductive principle, the proposed UCC-SWPDT system can charge multiple AUVs in seawater wirelessly at intervals of tens of centimeters.
2) Multiple bidirectional data transfer channels are constructed on the basis of multiple power transfer channels, which are capable of realizing the bidirectional communication function between the energy station and the AUV clusters. The transmission characteristics of the power channels and the bidirectional data channels are explored in detail and the crosstalk between them is analyzed.
3) The proposed UCC-SWPDT system has excellent misalignment characteristics and is capable of achieving stable power output and reliable communication at different vertical transmission distances and horizontal misalignment distances.

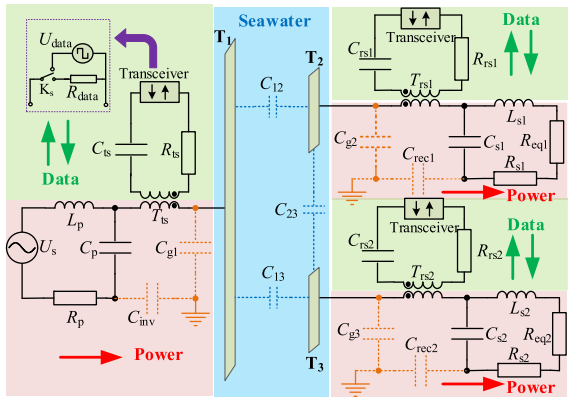

Fig. 2. Topology of the UCC-SWPDT system.

The rest of this article is organized as follows. In Section II, the topology of the UCC-SWPDT system is given and the working principle is outlined. The characterization of the power channels and the data channels is analyzed in Sections III and IV, respectively. DM interference and CM interference of the power channel to the data channel are analyzed in Section V. The modeling and simulation analysis of the coupling mechanism is presented in Section VI, and the parametric design flow of the UCC-SWPDT system is proposed. In Section VII, a prototype with a total power output of 200 W and a multiload data rate of 1 Mb/s is built. The feasibility of the proposed scheme is demonstrated. Finally, Section VIII concludes this article.

II. Overview of the System

The topology of the UCC-SWPDT system proposed in this article is shown in Fig. 2. T_1 is the metal plate at the transmitting side while T_2 and T_3 are the metal plates at the receiving side, which form the coupling capacitors C_{12}, C_{13}, and C_{23}, respectively. Based on the investigation of [26], the self-capacitance of the metal plate to the ground is C_{g1}, C_{g2}, and C_{g3}, respectively. Note that there are only two receiving devices given in Fig. 2 to simplify the analysis. In fact, the UCC-SWPDT system proposed in this article is suitable for charging and data transmission of more than two undersea devices. Theoretical analysis of more than two devices is also involved in the following sections.

For the power channel, U_s is the equivalent high-frequency power supply, which is composed of an H-bridge inverter. L_p is the resonant inductance of the transmitter, and C_p is the resonant capacitance of the transmitter, while R_p is the internal resistance of L_p. C_{inv} is the stray capacitance of the inverter to ground [23], [26]. At the receiving side, L_{si} ($i = 1, 2$) is the resonant inductance, and C_{si} ($i = 1, 2$) is the resonant capacitance, while R_{si} ($i = 1, 2$) is the internal resistance of L_{si}. R_{eqi} ($i = 1, 2$) is the equivalent load of the battery load R_{Li} ($i = 1, 2$) after impedance transforming by an H-bridge rectifier. C_{reci} ($i = 1, 2$) is the stray capacitance of the rectifier to ground [23], [26].

For the data channel, U_{data} is the equivalent power supply for transmitting data and R_{data} acquires the received data voltage and transfers it to the demodulation circuit for processing. The direction of data transmission is changed by switch K_s. U_{data},

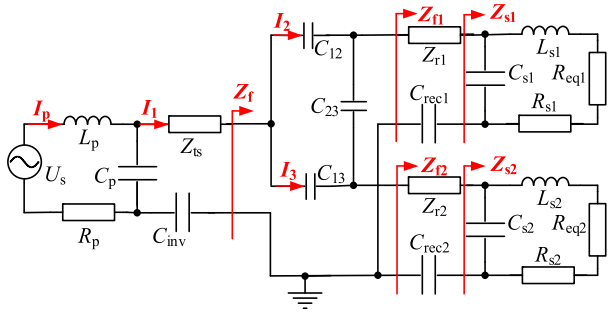

Fig. 3. Equivalent circuit of power channel.

R_{data}, and K_s constitute the data transceiver. C_{ts} is the resonant capacitance of the data loop at the power transmitting side and R_{ts} is the internal resistance of the loop. Data is coupled into the power channel with T_{ts}. At the power receiving side, data is coupled into the power channel with T_{rsi} $(i=1,2)$. C_{rsi} $(i=1,2)$ is the resonant capacitance of the data loop at the power receiving side, and R_{rsi} $(i=1,2)$ is the internal resistance of the loop. Also, the coupled metal plates are crucial to the UCC-SWPDT system, which determines the transfer power and efficiency of the power channel as well as the gain and SNR of the data channel. The detailed analysis and parameter design procedure will be given in Section VI.

III. Power Channel Analysis

The equivalent circuit of the power channel of UCC-SWPDT is shown in Fig. 3. C_{gi} $(i=1,2,3)$ is neglected in Fig. 3 because it is much smaller than the other capacitors in the power channel at the pF level [24]. Where Z_{ts}, Z_{r1}, and Z_{r2} are the equivalent impedance of the power channel to the data channel. Typically, the power channel operates in the kHz band while the data channel operates in the MHz band. C_{ts} and C_{rsi} are pF level. Hence, the data channel has a high impedance feature to the power channel. Z_t and Z_{rsi} $(i=1,2)$ can be expressed as

$$\begin{cases} Z_{ts}(\omega_p) \approx \mathrm{j}\omega_p L_{ts} \\ Z_{rsi}(\omega_p) \approx \mathrm{j}\omega_p L_{rsi} \end{cases} \tag{1}$$

where $\omega_{\mathrm{p}} = 2\pi f_p$, f_p is the operating frequency of the power channel while L_{ts} and L_{rsi} $(i=1,2)$ are the winding self-inductance of T_{ts} and T_{rsi}, respectively.

The equations of the circuit in which I_p and I_1 are involved are

$$(\mathrm{j}\omega_p L_p + 1/(\mathrm{j}\omega_p C_p) + R_p)\, I_p - 1/(\mathrm{j}\omega_p C_p) I_1 = U_s \tag{2}$$

$$(1/(\mathrm{j}\omega_p C_p) + 1/(\mathrm{j}\omega_p C_{inv}) + Z_t + Z_f)\, I_1 - 1/(\mathrm{j}\omega_p C_p) I_p = 0 \tag{3}$$

where Z_f is the port impedance given by the red arrows.

The resonance condition of the power channel is

$$\omega_p^2 L_p C_p = \omega_p^2 L_{s1} C_{s1} = \omega_p^2 L_{s2} C_{s2} = 1. \tag{4}$$

Combining (4) and (2), I_1 can be obtained that

$$I_1 = \mathrm{j}\omega_p C_p (R_p I_p - U_s) \approx -\mathrm{j}\omega_p C_p U_s. \tag{5}$$

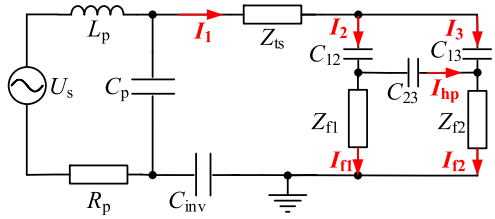

Fig. 4. Simplified equivalent circuit of the power channel.

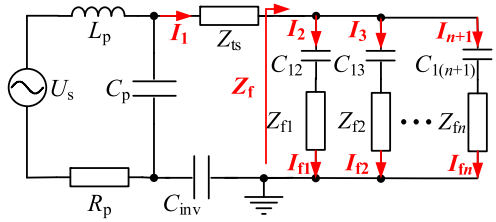

Fig. 5. Equivalent circuit of power channel with n receiving devices.

I_1 presents a constant current -j$\omega_p C_p U_s$ if the usually low R_p is neglected. This means that I_1 is determined by C_p and U_s, which is independent of the load R_{eqi} and the coupling capacitance C_{ij} $(i, j = 1, 2, 3, i{\neq}j)$. To further analyze the characteristics of the power channel, the impedance is given as follows:

$$Z_{si}(\omega_p) = \frac{\mathrm{j}\omega_p L_{si} + R_{eqi} + R_{si}}{\mathrm{j}\omega_p C_{si}(R_{eqi} + R_{si})}, (i = 1, 2) \tag{6}$$

$$Z_{fi}(\omega_p) = Z_{ri} + Z_{si} + 1/(\mathrm{j}\omega_p C_{reci}), (i = 1, 2)\,. \tag{7}$$

Based on the above derivation, a simplified equivalent circuit of the power channel is given in Fig. 4. The branch currents in Fig. 4 can be represented as follows:

$$\begin{cases} I_1 = I_2 + I_3 = I_{f1} + I_{f2} \\ I_2 = I_{f1} + I_{hp} \\ I_3 = I_{f2} - I_{hp} \end{cases} \tag{8}$$

where I_{hp} is the loop current flowing through the coupling capacitor C_{23} of the metal plates T_2 and T_3. It can be seen that if the loop current I_{hp} flows through C_{23}, then the system generates reactive power on the receiving side, which in turn reduces the efficiency of the system. In addition, since $I_1 = I_{\mathrm{f1}} + I_{\mathrm{f2}}$, I_1 at the transmitting side flows into Z_{f1} and Z_{f2}, and the loop current I_{hp} has essentially no effect on the total output power of the system. However, the presence of I_{hp} means that the electrical bridge in Fig. 4 is unbalanced, resulting in $I_{\mathrm{f1}} \neq \mathrm{I_{f2}}$ and the output power of each device at the receiving side is not equal.

Here, assuming that the metal plate at the receiving side and all load parameters are identical, $C_{12} = \mathrm{C_{13}}$, $Z_{\mathrm{f1}} = Z_{\mathrm{f2}}$. It is obvious that the electrical bridge in Fig. 4 will be balanced and $I_{hp} = 0$. Furthermore, the equivalent circuit of the system is shown in Fig. 5 when there are n $(n \geq 2)$ devices with the same parameters at the receiving side to be charged. The current I_{fi} at each receive port can be expressed as

$$I_{fi} = I_{f1} = I_{f2} = \cdots = I_{fn} = \frac{1}{n} I_1 = \frac{-\mathrm{j}\omega_p C_p U_s}{n}, (i = 1, 2, \ldots, n)\,. \tag{9}$$

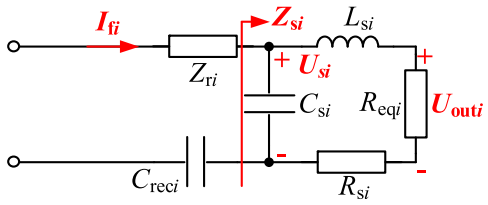

Fig. 6. Receiving port equivalent circuit of the power channel.

Then, Fig. 6 shows the receiving port equivalent circuit of the power channel. The port voltage U_{si} (i = 1,2,⋯,n) can be expressed as

$$U_{si} = I_{fi}Z_{si} = \frac{-C_pU_s\left(\mathrm{j}\omega_pL_{si} + R_{eqi} + R_{si}\right)}{nC_{si}\left(R_{eqi} + R_{si}\right)}. \tag{10}$$

The output voltage $U_{\mathrm{out}\,i}$ of each receiving port is

$$U_{outi} = \frac{R_{eqi}}{\mathrm{j}\omega_pL_{si} + R_{eqi} + R_{si}}U_{si} = \frac{-C_pU_sR_{eqi}}{nC_{si}\left(R_{eqi} + R_{si}\right)}. \tag{11}$$

Generally, the equivalent load resistance R_{eqi} is much larger than R_{si} and $U_{\mathrm{out}\,i}$ can be approximated as

$$U_{\mathrm{out}i} \approx \frac{-C_pU_s}{nC_{si}}. \tag{12}$$

In reality, R_{eqi} on the receiving side are not always equivalent. Different R_{eqi} leads to $I_{hp} \neq 0$, which in turn increases the reactive power of the system and reduces the efficiency. Therefore, it is possible to add the dc–dc circuit for impedance matching in the receiving side of the practical system to ensure that all R_{eqi} on the receiving side are the same as far as possible.

From the abovementioned equation, it can be seen that the output of the power channel has a constant voltage characteristic independent of the load R_{eqi} and coupled capacitance C_{1i} (i = 2,3,⋯, n). The output voltage of each receiving port is determined by C_p, $C_{si,}$ and the number of ports. This conclusion is obtained by neglecting R_p and R_{si}. The conditions for omitting R_p and R_{si} in Figs. 3 and 6 are

$$\begin{cases} Z_{ts}\left(\omega_p\right) + Z_f(\omega_p) + 1/(\mathrm{j}\omega_pC_{inv}) \gg R_p \\ R_{eqi} \gg R_{si}, (i = 1, 2)\,. \end{cases} \tag{13}$$

Significantly, in contrast to the inductive power transfer system, the output voltage of the system proposed in this article is approximately independent of the coupled capacitance, which implies that it has a very well misaligned characteristic. The detailed characterization of the misalignment is given in Section VI.

Also, the output power of each receiving port can be expressed as

$$P_{\mathrm{out}i} = \frac{C_p^2U_s^2R_{eqi}}{n^2C_{si}^2\left(R_{eqi} + R_{si}\right)^2}. \tag{14}$$

The port impedance Z_f in Fig. 5 can be shown as

$$Z_f\left(\omega_p\right) = n/(\mathrm{j}\omega_pC_{1i}) + nZ_{fi}, (i = 1, 2, \cdots, n)\,. \tag{15}$$

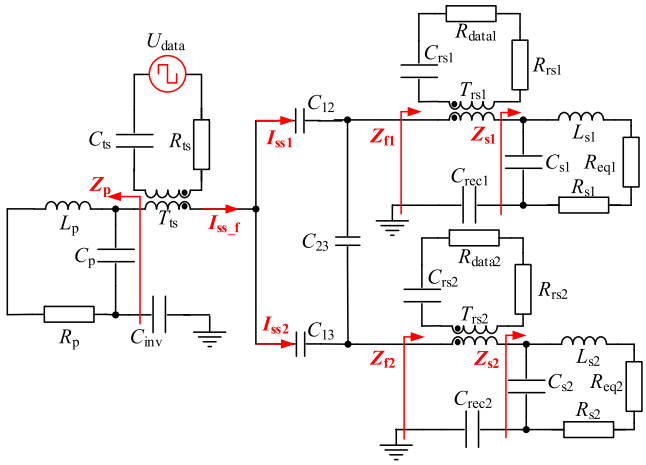

Fig. 7. Equivalent circuit of the forward data channel.

Combining (2)–(4) and (15), the input current I_p and transmission efficiency η_p can be obtained

$$\begin{cases} I_p = \frac{AU_s}{AR_p + \mathrm{j}\omega_pL_pC_{inv}}, A = C_{inv} + C_p + \mathrm{j}\omega_pC_p\left(Z_t + Z_f\right) \\ \eta_p = \frac{nP_{oui}}{U_sI_p} = \frac{C_p^2R_{eqi}(AR_p + \mathrm{j}\omega_pL_pC_{inv})}{nC_{si}^2(R_{eqi} + R_{si})^2A}. \end{cases} \tag{16}$$

IV. Data Channel Analysis

The UCC-SWPDT system proposed in this article switches the data transfer direction by switching Ks. The energy station sends instructions for all AUVs when the data is transferred in the forward direction. When data is transferred in the backward direction, each AUV uploads data to the energy station in a time-division mode. The forward channel and the backward channel of data transmission are analyzed separately in the following.

A. Forward Channel

The energy station sends information to all the receivers when the data is transferred in the forward direction. The equivalent circuit of the forward data channel is shown in Fig. 7. The impedance Z_p and Z_{si} (i = 1,2) of the data channel to the power channel can be represented as

$$Z_p\left(\omega_s\right) = \frac{\mathrm{j}\omega_sL_p + R_p}{1 - \omega_s^2L_pC_p + \mathrm{j}\omega_sC_pR_p} \tag{17}$$

$$Z_{si}\left(\omega_s\right) = \frac{\mathrm{j}\omega_sL_{si} + R_{eqi} + R_{si}}{1 - \omega_s^2L_{si}C_{si} + \mathrm{j}\omega_sC_{si}\left(R_{eqi} + R_{si}\right)} \tag{18}$$

where $\omega_{\mathrm{s}} = 2\pi f_s$, f_s is the operating frequency of the power channel.

Fig. 7 can be further equated to the simplified equivalent circuit shown in Fig. 8. Here, L_{ts1} and L_{ts2} are the primary and secondary self-inductance of the transformer T_{ts}, respectively, and M_{ts} is the mutual inductance between the primary and secondary sides. The resonant capacitance C_{ts} is satisfied as follows:

$$\omega_s^2L_{ts}C_{ts} = \omega_s^2L_{ts1}C_{ts} = \omega_s^2L_{ts2}C_{ts} = 1. \tag{19}$$

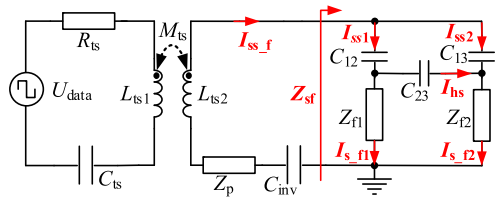

Fig. 8. Simplified equivalent circuit of the forward data channel.

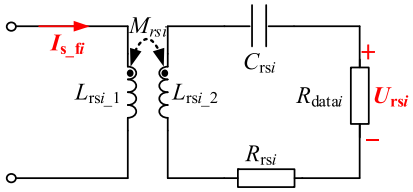

Fig. 9. Receiving port equivalent circuit of the forward data channel.

Typically, the internal resistances R_{ts} can be neglected since they are relatively low in the circuit. At this point, the current I_{ss_f} can be obtained as

$$I_{ss\_f} = \frac{U_{\text{data}}}{\text{j}\omega_s M_{ts}}. \tag{20}$$

In this case, the analysis of the circuit in Fig. 8 is consistent with the circuit in Fig. 4. Assuming that the parameters of each receiving port are equal, the loop circuit $I_{hs} = 0$ and the branch current I_{s_fi} can be represented as

$$\begin{aligned} I_{s\_fi} &= I_{s\_f1} = I_{s\_f2} = \cdots = I_{s\_fn} = \frac{1}{n} I_{ss\_f} \\ &= \frac{U_{\text{data}}}{\text{j}\omega_s M_{ts} n}, (i = 1, 2, \ldots, n). \end{aligned} \tag{21}$$

Then, Fig. 9 shows the receiving port equivalent circuit of the forward data channel. Here, L_{rsi_1} and L_{rsi_2} are the primary and secondary self-inductance of the transformer T_{rsi}, respectively, and M_{rsi} is the mutual inductance between the primary and secondary sides. The resonant capacitance C_{rsi} is satisfied as follows:

$$\omega_s^2 L_{rsi} C_{rsi} = \omega_s^2 L_{rsi\_1} C_{rsi} = \omega_s^2 L_{rsi\_2} C_{rsi} = 1. \tag{22}$$

Consequently, the voltage U_{rsi} of the sampling resistor $R_{\text{data}i}$ can be obtained as

$$\begin{aligned} U_{rsi} &= \frac{\text{j}\omega_s M_{rsi} R_{\text{data}i}}{R_{\text{data}i} + R_{rsi}} I_{s\_fi} \\ &= \frac{M_{rsi} R_{\text{data}i}}{n M_{ts} \left(R_{\text{data}i} + R_{rsi}\right)} U_{\text{data}}, (i = 1, 2, \cdots, n). \end{aligned} \tag{23}$$

The voltage gain G_{dfi} for the forward data channel is

$$G_{dfi}(\omega_s) = \frac{U_{rsi}}{U_{\text{data}}} = \frac{M_{rsi} R_{\text{data}i}}{n M_{ts} \left(R_{\text{data}i} + R_{rsi}\right)}, (i = 1, 2, \cdots, n). \tag{24}$$

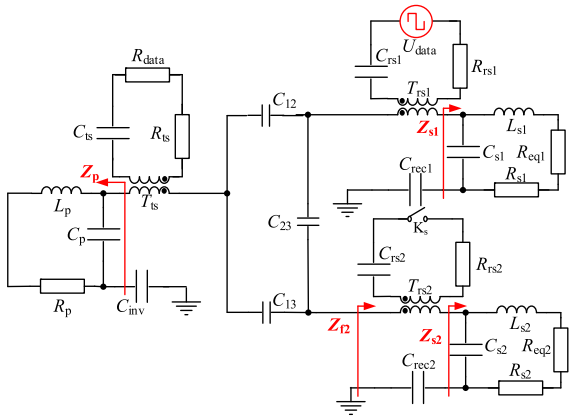

Fig. 10. Equivalent circuit of the back data channel.

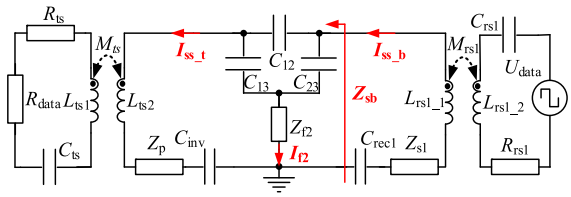

Fig. 11. Simplified equivalent circuit of the backward data channel.

B. Backward Channel

The communication system operates in time division multiplexing mode while each AUV uploads data to the energy station. Consequently, there is only one port on the receiving side that is excited by U_{data}, while the other ports are disconnected by Ks. The equivalent circuit of the backward data channel is presented in Fig. 10. Like the forward channel, the port impedance of the backward data channel to the power channel is as follows:

$$\begin{cases} Z_p(\omega_s) = \frac{\text{j}\omega_s L_p + R_p}{1 - \omega_s^2 L_p C_p + \text{j}\omega_s C_p R_p} \\ Z_{si}(\omega_s) = \frac{\text{j}\omega_s L_{si} + R_{eqi} + R_{si}}{1 - \omega_s^2 L_{si} C_{si} + \text{j}\omega_s C_{si}(R_{eqi} + R_{si})}, (i = 1, 2, \cdots, n) \\ Z_{fj}(\omega_s) = \frac{1}{\text{j}\omega_s C_{recj}} + Z_{sj} + L_{rsj}, (j = 2, \cdots, n). \end{cases} \tag{25}$$

A simplified equivalent circuit of the backward data channel is shown in Fig. 11, with $i = 1$, $n = 2$ as an illustration. Similar to I_{ss_f} in Fig. 8, I_{ss_b} can be expressed when R_{rs1} is neglected as

$$I_{ss\_b} = \frac{U_{\text{data}}}{\text{j}\omega_s M_{rsi}}. \tag{26}$$

In addition, it can be seen that a current I_{f2} flows across the impedance Z_{f2} at the receiving port where data is not uploaded. I_{ss_t} can be represented as

$$I_{ss\_t} = I_{ss\_b} - I_{f2}. \tag{27}$$

If $n > 2$, the presence of a parallel impedance Z_{fj} $(j > 3)$ on Z_{f2} leads to a larger I_{f2}, which will further reduce I_{ss_t}. Therefore, this article proposes that the receiving side of the data that has not been uploaded should be physically separated in the backward data transmission process to avoid severe degradation of the

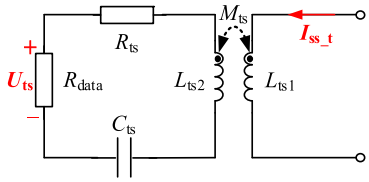

Fig. 12. Receiving port equivalent circuit of the backward data channel.

data gain. When the receiving side that has not uploaded data is disconnected, Z_{f2} is open and $I_{ss\_t} = I_{ss\_b}$.

Then, Fig. 12 shows the receiving port equivalent circuit of the backward data channel. The voltage U_{ts} of the sampling resistor R_{data} can be obtained as

$$U_{ts} = \frac{\mathrm{j}\omega_s M_{ts} R_{\mathrm{data}}}{R_{\mathrm{data}} + R_{ts}} I_{ss\_t} = \frac{M_{ts} R_{\mathrm{data}}}{M_{rsi}\left(R_{\mathrm{data}} + R_{ts}\right)} U_{\mathrm{data}}. \quad (28)$$

The voltage gain G_{db} for the backward data channel is

$$G_{db}\left(\omega_s\right) = \frac{U_{ts}}{U_{\mathrm{data}}} = \frac{M_{ts} R_{\mathrm{data}}}{M_{rsi}\left(R_{\mathrm{data}} + R_{ts}\right)}. \quad (29)$$

It should be noted that although the forward and backward data gains in (24) and (29) are independent of the coupling capacitance $C_{ij}\,(i,j=1,2,\cdots,n,i\neq j)$, this conclusion is obtained by neglecting R_{rsi} and R_{ts}. The conditions for omitting R_{rsi} and R_{ts} in Figs. 8 and 11 are

$$\begin{cases} Z_p\left(\omega_s\right) + 1/(\mathrm{j}\omega_s C_{inv}) + Z_{sf}\left(\omega_s\right) \gg R_{ts} \\ Z_{si}\left(\omega_s\right) + 1/(\mathrm{j}\omega_s C_{reci}) + Z_{sf}\left(\omega_s\right) \gg R_{rsi}, (i = 1, 2, \cdots, n). \end{cases} \quad (30)$$

V. Crosstalk Analysis

When data and power are transmitted simultaneously, the power channel is a source of interference to the data channel. In general, there are two main types of interference that can affect the reliability and stability of the communication system, which are DM interference and CM interference [20]. DM interference flows into the data loop through the coupling transformer while CM interference flows into the data loop through the parasitic capacitances. The DM interference and CM interference are analyzed separately in the following.

A. DM Interference

The equivalent circuits of DM interference for the forward channel and backward channel are shown in Fig. 13(a) and (b), respectively. In the forward channel, the current I_{fi} of the power channel flows through the coupling transformer T_{rsi} to generate the interference voltage $U_{\mathrm{DM\_}f}$ on $R_{\mathrm{data}i}$. In the backward channel, the current I_1 of the power channel flows through the coupling transformer T_{ts} to generate the interference voltage $U_{\mathrm{DM\_}b}$ on R_{data}. DM noise gain $G_{\mathrm{DM\_}f}$ and $G_{\mathrm{DM\_}b}$ can be presented as

$$\begin{cases} G_{\mathrm{DM\_}f}\left(\omega_p\right) = \frac{U_{\mathrm{DM\_}f}}{U_s} = \frac{\omega_p^2 C_p M_{rsi} R_{\mathrm{data}i}}{n[\mathrm{j}\omega_p L_{rsi} + 1/(\mathrm{j}\omega_p C_{rsi}) + R_{rsi} + R_{\mathrm{data}i}]} \\ G_{\mathrm{DM\_}b}\left(\omega_p\right) = \frac{U_{\mathrm{DM\_}b}}{U_s} = \frac{\omega_p^2 C_p M_{ts} R_{\mathrm{data}}}{\mathrm{j}\omega_p L_{ts} + 1/(\mathrm{j}\omega_p C_{ts}) + R_{ts} + R_{\mathrm{data}}}. \end{cases} \quad (31)$$

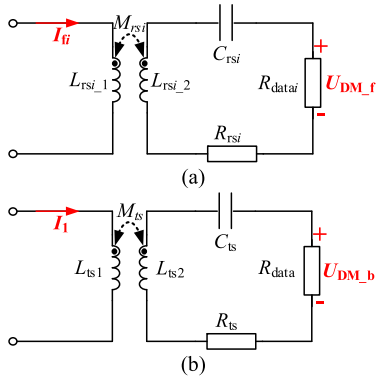

Fig. 13. Equivalent circuit of DM interference. (a) Forward channel. (b) Backward channel.

The DM $\mathrm{SNR}_{\mathrm{DM\_}f}$ and $\mathrm{SNR}_{\mathrm{DM\_}b}$ can be expressed as

$$\begin{cases} \mathrm{SNR}_{\mathrm{DM\_}f} = \frac{U_{\mathrm{data}} G_{dfi}(\omega_s)}{U_s G_{\mathrm{DM\_}f}(\omega_p)} \\ \qquad = \frac{U_{\mathrm{data}}}{U_s} \frac{\mathrm{j}\omega_p L_{rsi} + 1/(\mathrm{j}\omega_p C_{rsi}) + R_{rsi} + R_{\mathrm{data}i}}{\omega_p^2 C_p M_{ts}(R_{\mathrm{data}i} + R_{rsi})} \\ \mathrm{SNR}_{\mathrm{DM\_}b} = \frac{U_{\mathrm{data}} G_{db}(\omega_s)}{U_s G_{\mathrm{DM\_}b}(\omega_p)} \\ \qquad = \frac{U_{\mathrm{data}}}{U_s} \frac{\mathrm{j}\omega_p L_{ts} + 1/(\mathrm{j}\omega_p C_{ts}) + R_{ts} + R_{\mathrm{data}}}{\omega_p^2 C_p M_{rsi}(R_{\mathrm{data}} + R_{ts})}. \end{cases} \quad (32)$$

B. CM Interference

The equivalent circuit of CM interference for all CM currents path distribution is shown in Fig. 14(a). In this case, all CM current paths and directions are marked with red dashed lines and red arrows, which are formed into a complete loop through the parasitic capacitances of the nodes to earth in the UCC-SWPDT system. Additionally, the green line highlights the CM currents of the data circuits at the transmitting and receiving sides. To facilitate the analysis of CM interference, R_{data} and $R_{\mathrm{data}i}$ are placed in the same circuit. It should be noted, however, that only one of them can be available at any given moment.

The equivalent circuits for CM interference in the forward and backward data channels are presented in Fig. 14(b) and (c), respectively. In Fig. 14(b) and (c), U_{SA} and U_{SB} is the switching moment interference voltage generated at nodes A and B in Fig. 14(a). C_{gA} and C_{gB} are the parasitic capacitances of nodes A and B to the earth. C_Y is the Y capacitance of the dc power supply U_{in}. C_{t_rs} and C_{r_rs} are the interlayer capacitances of the coupling transformers T_{ts} and T_{rsi}, respectively. C_{gt} is the parasitic capacitance of the data circuit at the transmitting side to the earth, which is coupled to the earth through the power supply of the data circuit. C_{gs} is the parasitic capacitance of the data circuit at the receiving side to the earth, which has a similar coupling path to the earth as the transmitting side. It follows that there will be CM interference $U_{\mathrm{cm\_}f}$ on $R_{\mathrm{data}i}$ and CM interference $U_{\mathrm{cm\_}b}$ on R_{data}. The parasitic capacitances mentioned above are difficult to be measured accurately thus $U_{\mathrm{cm\_}f}$ and $U_{\mathrm{CM\_}b}$ are hardly to be analyzed precisely and quantitatively. In the meantime, the parasitic capacitances generated by the communication circuits that pass through the weak power supply to the ground cannot be eliminated. In light of the aforementioned considerations, $U_{\mathrm{CM\_}f}$ and $U_{\mathrm{CM\_}b}$ are filtered with a highly attenuated band-pass filter (BPF) in this

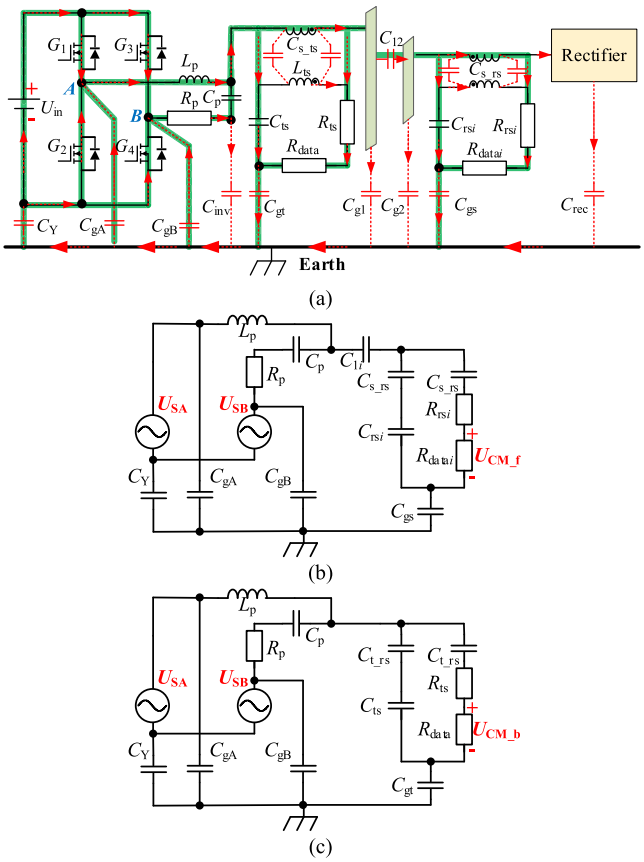

Fig. 14. Equivalent circuit of CM interference. (a) All CM currents path distribution. (b) Equivalent circuit of CM interference for forward channel. (c) Equivalent circuit of CM interference for backward channel.

article. The properties of the BPF is given in the experimental section.

C. Interference of High-Order Harmonics on Power and Data Channel

In the SCC-WPT system, a certain degree of high-order harmonics exists in the system due to the dispersion of stray capacitances. Although there is no literature report on the reasons for the generation of high-order harmonics for the time being, this article analyses the effects of high-order harmonics on the power channel and the data channel in order to guide the design of the UCC-SWPDT system.

Unlike inductive power transfer, capacitive power transfer relies on the voltage between metal plates to form a coupled electric field for energy transmission. The voltage between the metal plates is the key to exciting the high frequency electric field. Although the waveforms in the experiment show that there are high-order harmonics in the current flowing through the metal plates, the output power and transmission efficiency of the power channel are basically consistent with the theoretical analysis [23]. It can be seen that the high-order harmonics have a minor impact on the transmission performance of the power channel.

The interference of high-order harmonics flowing through the metal plates to the data channel can be classified as DM

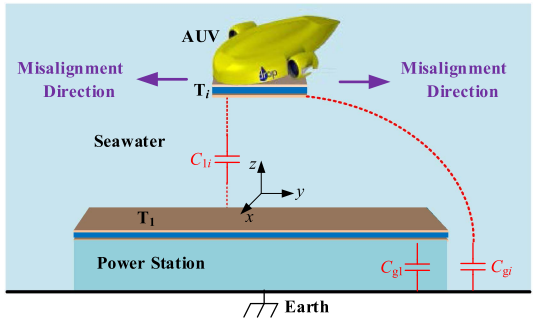

Fig. 15. Schematic modeling of the coupling mechanism.

interference. Although there is the rich spectrum in the DM interference, the carrier component of the data channel can be obtained from the interference using a bandpass filter. Therefore, DM interference can be easily filtered out. In contrast, CM interference affects the data channel much more than DM interference affects the data channel, and it is difficult to be effectively attenuated by bandpass filter. It is the fundamental reason for data transmission errors. Although the high-order harmonics generate DM interference to the data channel, this can be effectively filtered out. Therefore, the interference generated by the high-order harmonics to the data channel is very limited.

In future research, it is crucial to investigate the generation mechanism of high-order harmonics in the SCC-WPT system, which will help to explore the system in depth and apply it to more applications.

VI. Coupling Mechanism Analysis and Parameter Design

The preceding sections have analyzed the UCC-SWPDT system from the perspective of equivalent circuits. In addition, the role of the coupling mechanism in the UCC-SWPDT system is of particular significance. The subsequent content presents a model of the coupling mechanism and its associated misalignment characteristics, as well as a parametric design methodology for the UCC-SWPDT system.

A. Modeling and Misalignment Characterization

The schematic modeling of the coupling mechanism in seawater is shown in Fig. 15. The metal plate T_1 at the transmitting side is placed on the upper surface of the power station. Only an AUV and the metal plate T_i ($i = 2, 3, \cdots, n$) are given in Fig. 15 for clarity of the model. It can be observed from (9) that the coupling capacitances between the metal plates at the receiving side do not result in loop currents and do not affect the output power, provided that the parameters of the devices at the receiving side are consistent. Accordingly, the coupling characteristics between T_1 and a receiving-side metal plate T_i are analyzed.

The capacitance between T_1 and T_i is C_{1i}. The parasitic capacitances of T_1 and T_i to earth are C_{g1} and C_{gi}, respectively. Based on the investigation in [23], $C_{1i} \gg C_{g1}$ and $C_{1i} \gg C_{gi}$.

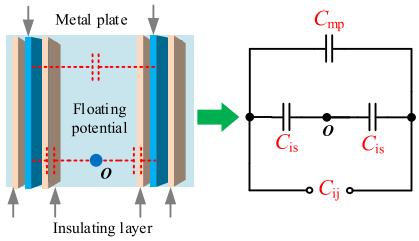

Fig. 16. Schematic modeling of two metal plates.

The major coupling path of the UCC-SWPDT system is constructed by C_{1i}. The schematic modeling of two metal plates covered by the insulating layer and placed in seawater is shown in Fig. 16. Typically, seawater has a conductivity of 3–5 S/m and can be approximated as a good conductor. At this point, there are three capacitances present in Fig. 16, which are the coupling capacitance C_{is} with the two metal plates to seawater through the insulating layer and the capacitance C_{mp} between the two metal plates.

In this case, seawater can be regarded as a floating potential that connects two C_{is} in a series. The equivalent circuit for the capacitance C_{ij} between two metal plates is modeled in Fig. 16. C_{ij} can be expressed as follows:

$$C_{ij} = C_{mp} + \frac{C_{is}}{2} \tag{33}$$

where C_{mp} can be obtained according to the following equation:

$$C_{mp} = \frac{\varepsilon_0 \varepsilon_{\text{seawater}} S_{\text{plate}}}{D}. \tag{34}$$

Among them, ε_0 is the dielectric constant in vacuum, which has a value of 8.85 $\times$ 10^{-12} F/m. $\varepsilon_{\text{seawater}}$ is the permittivity of seawater, which has a value of 81. S_{plate} is the orthogonal area between the metal plates and D is the transmission distance between the metal plates. In general, when D is greater than the size of metal plates, C_{mp} is at the pF level. Comparatively, C_{is} is determined by the thickness as well as the permittivity of the insulating layer and the surface area of the metal plates. The thickness of the insulating layer is at the μm level if the insulating layer is made of PE plastic film, then the value of C_{is} is at the nF level.

To validate the abovementioned analysis, a finite element simulation model is built in Fig. 17. The dimensions of T_1 are 40 cm $\times$ 40 cm $\times$ 1 mm and the dimension T_i is 40 cm $\times$ 20 cm $\times$ 1 mm. The thickness of the insulation layer is 20 μm. The excitation voltage between the metal plates is 100 V. When D = 30 cm, Δy = 0 cm, C_{ij} = 4.729 nF; when D = 30 cm, Δy = $\pm$40 cm, C_{ij} = 4.713 nF. Correspondingly, when D = 60 cm, Δy = 0 cm, C_{ij} = 4.710 nF; when D = 60 cm, Δy = $\pm$40 cm, C_{ij} = 4.701 nF. The value of C_{ij} is observed to exhibit minimal fluctuations regardless of misalignment in the y-direction or alteration in transmission distance. Consequently, such changes have a minimal impact on the UCC-SWPDT system. This phenomenon can be attributed to the fact that the value of C_{mp} is decreased during misalignment, while the larger C_{is} is hardly affected. Consequently, C_{ij} exhibits excellent antimisalignment characteristics in the misaligned scenario.

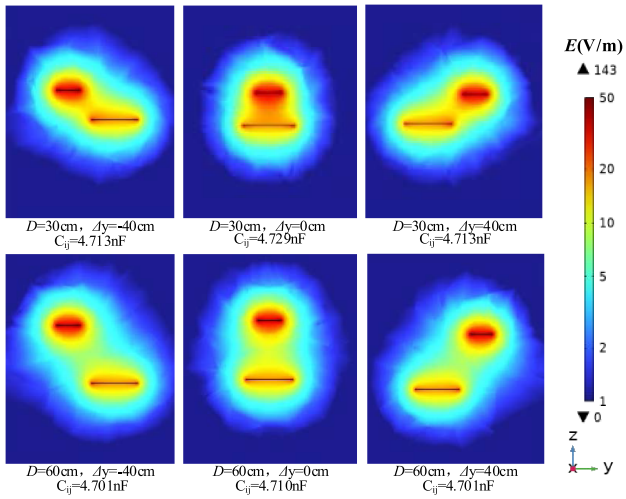

Fig. 17. Simulation for the electric field of the metal plate in seawater.

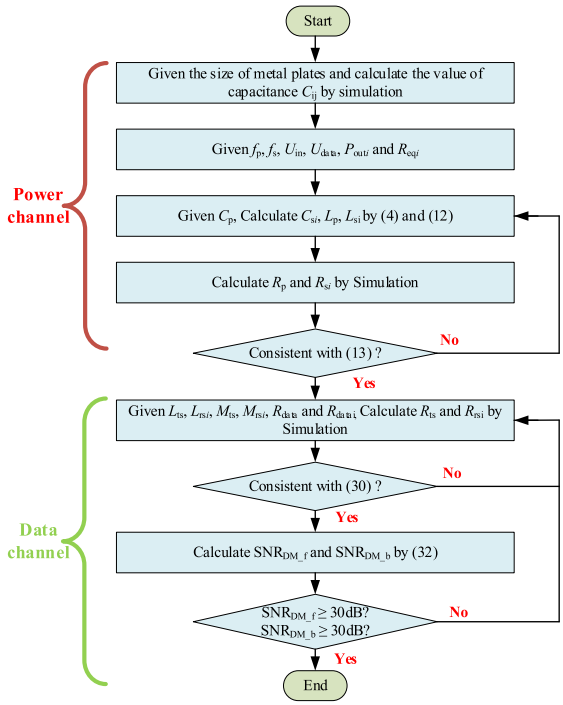

Fig. 18. Flowchart of parameters design.

B. Procedure of Parametric Design

The flowchart of parameters design for the UCC-SWPDT system is shown in Fig. 18. To begin with, given the rated frequency f_p and f_s, the input voltage U_s, the output power $P_{\text{out}\,i}$ for each output channel and the equivalent load $R_{\text{eq}\,i}$. Then, given C_p and calculate $C_{\text{s}i}$, L_{p}, and $L_{\text{s}i}$ according to (4) and (12). The most significant percentage of R_p and R_{si} is the internal resistance of L_p and $L_{\text{s}i}$. The values of R_p and $R_{\text{s}\,i}$ are calculated by carrying out finite element modeling and simulation of L_p and $L_{\text{s}i}$. It is emphasized that a value greater than 100 is chosen in this article as a condition for (13) and (30). This can be expressed

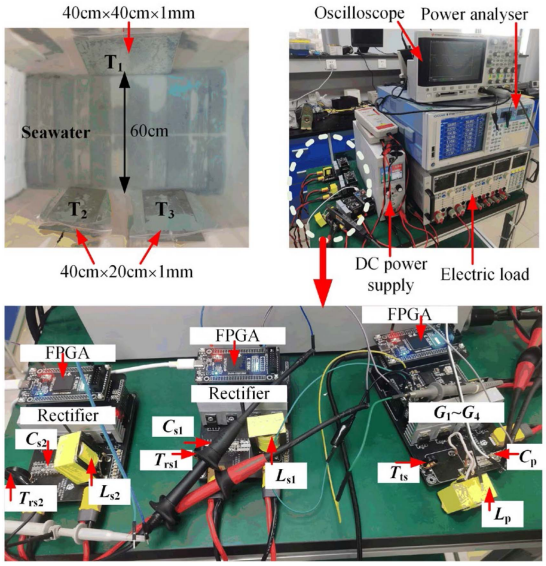

Fig. 19. Built prototype system.

as follows:

$$\begin{cases} Z_{ts}(\omega_p) + Z_f(\omega_p) + 1/(\mathrm{j}\omega_p C_{inv}) \geq 100R_p \\ R_{eqi} \geq 100R_{si} \end{cases} \tag{35}$$

$$\begin{cases} Z_p(\omega_s) + 1/(\mathrm{j}\omega_s C_{inv}) + Z_{sf}(\omega_s) \geq 100R_{ts} \\ Z_{si}(\omega_s) + 1/(\mathrm{j}\omega_s C_{reci}) + Z_{sf}(\omega_s) \geq 100R_{rsi} \end{cases}. \tag{36}$$

If the provided value satisfies the criterion of (35), then the design task for the power channel is complete; otherwise, the value of C_{p} is regiven, and the aforementioned procedure is repeated. Subsequently, the corresponding parameters of the data channel are calculated to ascertain whether they satisfy (36) as well as $\mathrm{SNR}_{\mathrm{DM}\_f}$ and $\mathrm{SNR}_{\mathrm{DM}\_b}$ are greater than 30 dB. The data channel comprises a multitude of parameters, which can be designed and optimized using a multiobjective optimization algorithm. Once the above conditions have been met, the parameter configuration of the data channel is deemed complete.

VII. Experimental Verification

A. Experimental Setup

In this section, a prototype with metal plates placed in seawater demonstrates the feasibility of the UCC-SWPDT system proposed in this article, as shown in Fig. 19. Among them, the size of the metal plate T_1 at the transmitting side is 40 cm × 40 cm × 1 mm and the size of the metal plate T_2 (T_3) at the receiving side is 40 cm × 20 cm × 1 mm, which is covered with a polythene material of 20 μm thickness for insulation. The distance between the transmitting side and the receiving side is 20 cm–60 cm. T_1,T_2, and T_3 are placed in a tank containing seawater. The conductivity of seawater is 4 S/m.

The field programmable gate array (FPGA) is XC6SLX16, which is used in modulation and demodulation for data channels. G_1–G_4 are IRFB4020 and the rectifier is composed of STPS20200C. Some critical components are labeled in Fig. 19. Since the coupling capacitance of the metal plates in seawater is at the nF level due to the high dielectric constant of seawater, a lower operating frequency of 200 kHz is selected for the power channel rather than the MHz level used in conventional CPT systems. In addition, lower frequency of the power channel can cause the size of the compensation inductor to increase dramatically. The data rate is set to 1 Mb/s and the carrier frequency for the data channel is 10 MHz. Because higher carrier frequencies will increase the complexity of sampling and data processing. Also, consistent with the approach in [23], Y capacitances of the power supply and the electronic load are used as C_{inv} and C_{reci} ($i = 1, 2$) in the channel. The parameters of the prototype are listed in Table I.

TABLE I
Parameter Values of the Prototype

Parameters	Values
U_{in}, U_{data} (V)	72, 10
R_{L1}, R_{L2}, R_{p}, R_{s1}, R_{s2} (Ω)	12, 12, 0.23, 0.24, 0.24
R_{ts}, R_{rsi} (Ω)	1.2, 1.2
L_{p}, L_{s1}, L_{s2} (μH)	92.1, 100.5, 100.5,
L_{ts}, L_{rsi}, M_{ts}, M_{rsi} (μH)	3.1, 3.1, 1.5, 1.5
C_{p}, C_{s1}, C_{s2}, C_{inv}, C_{reci} (nF)	6.87, 6.28, 6.28, 3.3, 1.5
C_{ts}, C_{rs}, C_{12}, C_{13}, C_{23} (nF)	0.085, 0.085, 5.2, 5.2, 4.6
f_p,f_s	200 kHz, 10 MHz
Conductivity of seawater	4 S/m

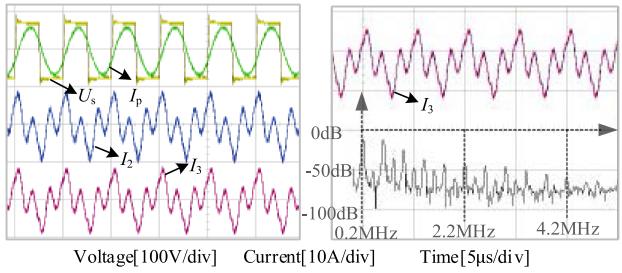

Fig. 20. Operating waveforms of the power channel.

B. Power Transfer

The operating waveforms of the power channel are shown in Fig. 20. The phase of U_s and I_p is identical, and I_p is slightly inductive to achieve the zero voltage switching state. Given that the parameters of the channels in which T_2 and T_3 are located are identical, the amplitude and phase of I_2 and I_3 are also identical. This indicates that there is no loop current in capacitor C_{23} between the two metal plates at the receiving side. It is consistent with the theoretical analysis in Section III. Nevertheless, it should be noted that I_2 and I_3 contain the larger third and fifth harmonics. The current research results do not provide a reasonable explanation of the harmonic generation principle. Consequently, further research is recommended to gain a more profound insight into the underlying mechanisms.

Fig. 21 presents the performance statistics of the power channel. When the load resistance R_L is increased from 12 Ω to 20 Ω, the output voltages of the channels where T_2 and T_3 are located are basically equal and approximately show constant voltage characteristics. Meanwhile, the output power of the channel

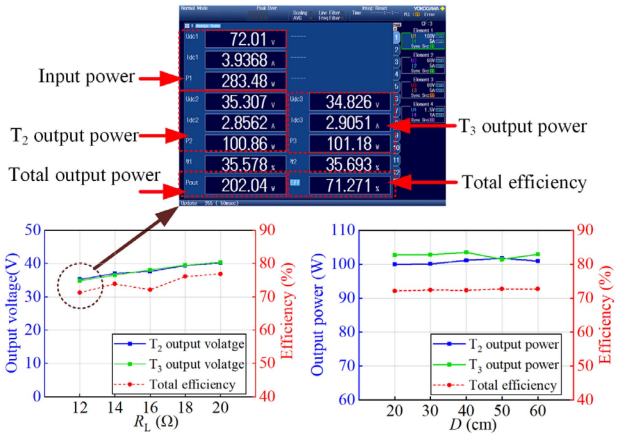

Fig. 21. Output statistics of the power channel.

where T_2 and T_3 are located is maintained at about 100 W when the transmission distance D is increased from 20 cm to 60 cm. The above experimental results demonstrate the correctness of (12) and the highly excellent anti-misalignment characteristics of the proposed system.

The data in Fig. 21 presents the efficiency measurements of the UCC-SWPDT system, which refers to the efficiency of the transmission from the transmitting side dc to the receiving side dc. When R_L is 12 Ω, the output power of the channel where T_2 is located is 100.86 W, and the output power of the channel where T_3 is located is 101.18 W. The total output power of the system is 202.04 W, and the transfer efficiency is 71.271%.

C. Data Transfer

The operating waveforms of the data channels are presented in Fig. 22. In this article, modulation and demodulation of the data channel are implemented with differential phase shift keying (DPSK) scheme. The DPSK modulated waveforms for the forward data channel are shown in Fig. 22(a). A frame of serial data "01011010" represents the data TX_f to be sent in the forward data channel of the FPGA. $U_{\rm data}$ is the high-frequency modulated signal output from the power amplifier. U_{rs1} and U_{rs2} are the received signals obtained on the sampling resistors $R_{\rm data1}$ and $R_{\rm data2}$, whose amplitudes are in accordance with the theoretical derivation of (23).

The demodulated waveforms for the forward data channel are given in Fig. 22(b). RX_{f1} and RX_{f2} are the two demodulated data at the receiving sides, respectively, which correspond to the transmit data TX_f and have a certain delay. The delay between RX_{f1} and RX_{f2} is due to the use of two incompletely identical FPGA.

Fig. 22(c) shows the operating waveforms of the backward data channel. TX_b is the data to be sent from the backward data channel and $U_{\rm data}$ is the modulated signal output from the power amplifier. $U_{\rm ts}$ is the signal collected on the resistance $R_{\rm data}$ and RX_b is the data obtained after demodulation by the FPGA at the transmitting side. The above experimental results demonstrate that the proposed UCC-SWPDT system is capable of forward multiload data transmission as well as backward data upload.

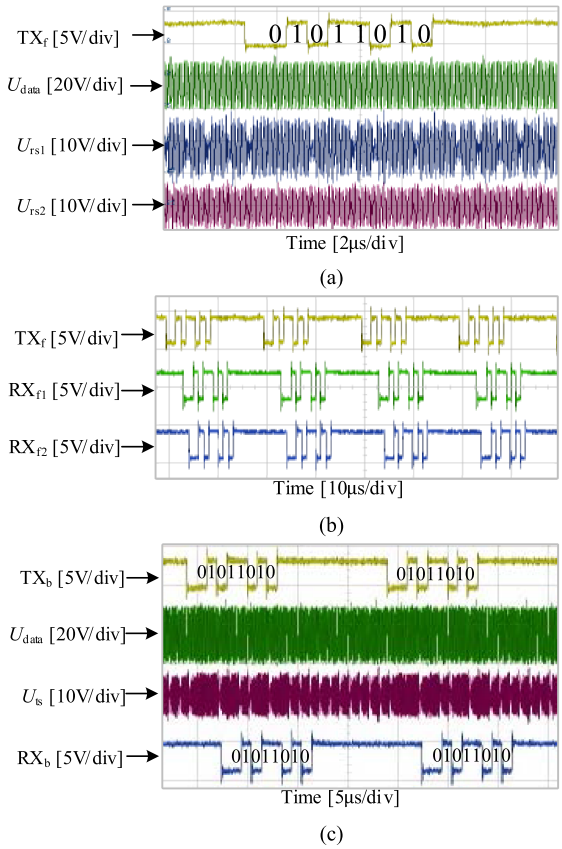

Fig. 22. Operating waveforms of the data channel. (a) Modulated waveforms of the forward data channel. (b) Demodulated waveforms of the forward data channel. (c) Operating waveforms of the backward data channel.

D. Simultaneous Power and Data Transfer

Fig. 23 shows the operating waveforms while power and data are transferred synchronously. The demodulated waveforms when the power is transmitted synchronously with the data in the forward direction are shown in Fig. 23(a). At this point, the amplitude of $U_{\rm s}$ is 72 V and the power transmitted in the channels where T_2 and T_3 are located is 100.86 W and 101.18 W, respectively, as shown in Fig. 21. Both output channels are capable of successfully demodulating baseband data from the transmitting side. The data rate is up to 1 Mb/s.

The sampled waveforms for forward data transmission are shown in Fig. 23(b). U_{rs1} is the waveform ON $R_{\rm data1}$ and U_{rs1_bpf} is the waveform after being filtered by the BPF. The center frequency of BPF is 10 MHz and bandwidth $B_{\rm filter}$ is 800 kHz, as shown in Fig. 24. Based on the analysis in Section V, it appears that U_{rs1} is interfering with DM noise and CM noise. DM interference is mainly dominated by a frequency of 200 kHz, which is the operating frequency f_p of the power channel. The CM interference is determined by the parasitic parameters shown in Fig. 14, which have a wide range of frequencies. The spectrum of U_{rs1} and U_{rs1_bpf} is shown in Fig. 23(c). As can be seen from the places marked in the red dotted line, after BPF, both DM and CM interferences within 0.2 MHz–10 MHz are well filtered out. Fig. 23(d) displays the modulation and demodulation waveforms during backward data transmission. Compared to the forward

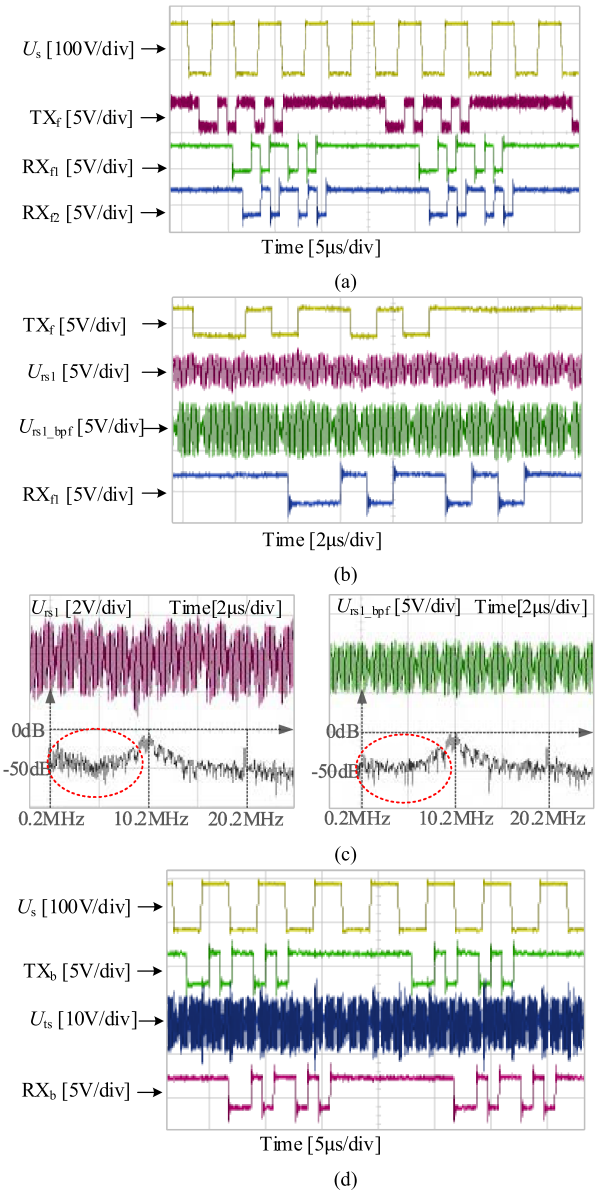

Fig. 23. Operating waveforms for simultaneous transmission of power and data. (a) Demodulated waveforms for forward data transmission. (b) Sampled waveforms for forward data transmission. (c) Spectrum of sampled waveforms. (d) Modulation and demodulation waveforms for backward data transmission.

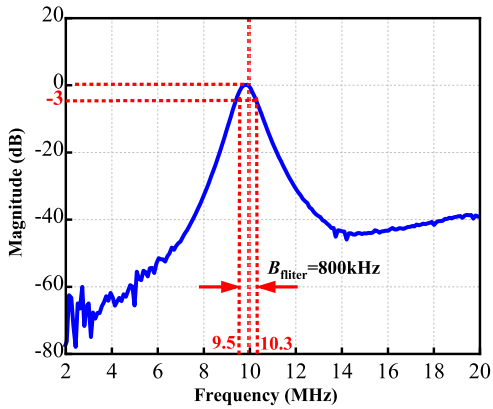

Fig. 24. Magnitude-frequency curve of BPF.

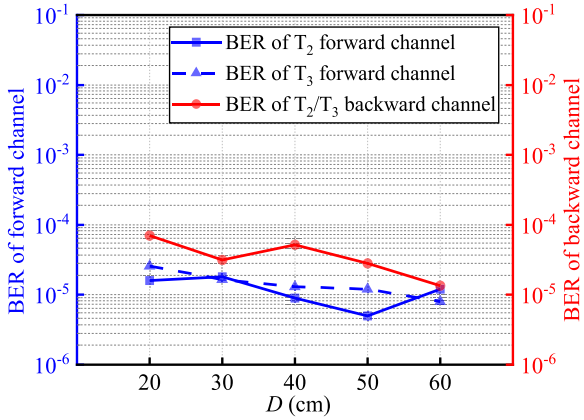

Fig. 25. BER statistics for data channels.

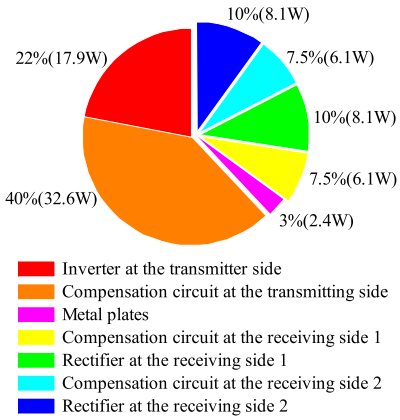

Fig. 26. Loss percentage of the UCC-SWPDT system.

channel, because R_{data} is closer to the inverter, the voltage U_{ts} on R_{data} has more interference compared to U_{rs1} and U_{rs2}.

The bit error rate (BER) of the data shown in Fig. 25 is counted to more clearly assess the impact of interference on communications. Overall, BER is less than 1e-4 for both forward and backward data channels when D is increased from 20 cm to 60 cm, indicating that the communication link proposed in this article has good reliability as well as excellent antimisalignment performance. Furthermore, the BER of the backward data channel is slightly higher than the BER of the forward data channels, due to the fact that the inverter generates more DM and CM interference at the transmitting side.

E. Power Loss Analysis

To investigate the power loss distribution of the UCC-SWPDT system, this article measured the power loss percentage of each circuit in the system with the power analyzer, as shown in Fig. 26. Because the parameters of the two receiving sides are set to be the same in this article, the losses of the compensation circuits and the rectifiers at the receiving side account for an equal proportion of the total losses, which are 7.5% (6.1 W) and 10% (8.1 W), respectively. The loss of the inverter at the transmitting side is 22% (17.9 W) of the total loss. The largest proportion of losses is in the compensation circuit at the transmitting side, up to 40%

TABLE II
COMPARISON WITH PREVIOUS WORK

Reference	Coupling mechanism	Output power	Transfer distance	Data rate (Forward/Backward)	Transfer medium	Number of load
[4]@2023	Coil taps (inductive)	518 W	3 cm	500 kb/s and 700 kb/s	Seawater	1
[6]@2023	Coil (inductive)	N/A	N/A	1.25 Mb/s and N/A	Air	2
[11]@2023	Coil (inductive)	936 W	N/A	8.5 kb/s and 8.5 kb/s	Seawater	1
[18]@2022	Coil (inductive)	500 W	3 cm	600 kb/s and 600 kb/s	Air	1
[19]@2024	Metal plate (capacitive)	460W	20 cm	N/A and 19.2 kb/s	Air	1
[20]@2024	Coil (inductive)	3.3 kW	N/A	N/A and 115.2 kb/s	Air	1
[21]@2024	Coil taps (inductive)	1.1 kW	6 cm	2 Mb/s and 2 Mb/s	Seawater	1
[23]@2024	Metal plate (capacitive)	300 W	1 m	500 kb/s and 500 kb/s	Seawater	1
Proposed	Metal plate (capacitive)	200 W	20~60 cm	1 Mb/s and 1 Mb/s	Seawater	≥2

N/A refers to the fact that the item is not available in the references.

(32.6 W). This is attributed to the high internal resistance of the inductor for primary side compensation, which poses a challenge to its heat dissipation.

F. Discussion

A comprehensive comparison of the UCC-SWPDT system with previous work is shown in Table II. The previous research primarily concentrated on examining a single load, which limited the applicability of the findings to more complex scenarios. In contrast, the research presented in this article extends its focus to encompass multiload scenarios, thereby broadening the scope and relevance of the investigation. The UCC-SWPDT system proposed herein offers distinct advantages when evaluated against key performance criteria. Specifically, it demonstrates improved transmission distance, enhanced communication rates, and greater capacity for handling multiple loads simultaneously. These advantages indicate that the proposed system is well-suited for practical applications involving multiple loads, extending the range of applications of SWPDT systems compared to previous researches.

VIII. CONCLUSION

This article presents a UCC-SWPDT system that can be applied in submerged multiload scenarios. The power and data channels of the system are modeled and analyzed in detail. Meanwhile, the modeling of the coupling mechanism and the parameter design flow are shown. Finally, a prototype with a total output power of 200 W and a bidirectional data rate of 1 Mb/s demonstrates the practicability of the system in submerged multiload scenarios. Future investigations will attempt to improve the power and data rate of the system.

REFERENCES

[1] T. Li, Z. Sun, Y. Wang, J. Mai, and D. Xu, "An underwater simultaneous wireless power and data transfer system with 1-Mbps full-duplex communication link," *IEEE Trans. Ind. Inform.*, vol. 20, no. 2, pp. 2620–2631, Feb. 2024.

[2] Z. Chen, X. Zhang, F. Xu, M. Li, Z. Yuan, and Q. Yang, "Wide rotation-misalignment-tolerance design of magnetic coupled structure for AUVs wireless charging system," *IEEE Trans. Ind. Electron.*, vol. 71, no. 11, pp. 14086–14096, Nov. 2024, doi: 10.1109/TIE.2024.3382978.

[3] L. Yang et al., "Comparison survey of effects of hull on AUVs for underwater capacitive wireless power transfer system and underwater inductive wireless power transfer system," *IEEE Access*, vol. 10, pp. 125401–125410, 2022.

[4] Y. Wang, T. Li, M. Zeng, J. Mai, P. Gu, and D. Xu, "An underwater simultaneous wireless power and data transfer system for AUV with high-rate full-duplex communication," *IEEE Trans. Power Electron.*, vol. 38, no. 1, pp. 619–633, Jan. 2023.

[5] L. Tan et al., "Power stability optimization design of three-dimensional wireless power transmission system in multi-load application scenarios," *IEEE Access*, vol. 8, pp. 91843–91854, 2020.

[6] P. Luo, F. Liu, and X. Chen, "Multi-port full-duplex simultaneous wireless information/power transfer method based on 4PAM modulation scheme with 1.25Mbps data rate," in *Proc. IEEE 14th Int. Symp. Power Electron. Distrib. Gener. Syst.*, 2023, pp. 525–530.

[7] W. Xiong, F. Jiang, Z. Liu, Q. Zhu, and M. Su, "A hybrid-frequency-based multi-load wireless power transfer system with constant current or voltage outputs," *IEEE J. Emerg. Sel. Topics Power Electron.*, vol. 12, no. 1, pp. 1150–1160, Feb. 2024.

[8] Z. Liu, H. Hu, Y. -G. Su, Y. Sun, F. Chen, and P. Deng, "A double-receiver compact SCC-WPT system with CV/CC output for mobile devices charging/supply," *IEEE Trans. Power Electron.*, vol. 38, no. 7, pp. 9230–9245, Jul. 2023.

[9] Z. Yan et al., "Frequency optimization of a loosely coupled underwater wireless power transfer system considering eddy current loss," *IEEE Trans. Ind. Electron.*, vol. 66, no. 5, pp. 3468–3476, May 2019.

[10] C. Da, L. Wang, F. Li, C. Tao, and Y. Zhang, "Analysis of undersea simultaneous wireless power and 1 Mb/s data rate transfer system based on DDQ coil," *IEEE Trans. Power Electron.*, vol. 38, no. 10, pp. 11814–11825, Oct. 2023.

[11] C. Cai, J. Li, S. Wu, Z. Qin, W. Chai, and S. Yang, "A bipolar and unipolar magnetic channel multiplexed WPT system with simultaneous full-duplex communication for autonomous underwater vehicles," *IEEE Trans. Power Electron.*, vol. 38, no. 12, pp. 15086–15090, Dec. 2023.

[12] Y. Luo, Y. Yang, H. Hong, and Z. Dai, "A simultaneous wireless power and data transfer system with full-duplex mode for underwater wireless sensor networks," *IEEE Sensors J.*, vol. 24, no. 8, pp. 12570–12583, Apr. 2024.

[13] P. Guo, R. Yuan, C. Cai, H. Lin, and L. Yang, "High-data-frequency-ratio information transmission method for fast dynamic response SWPIT systems based on DASK modulation," *IEEE J. Emerg. Sel. Topics Power Electron.*, vol. 9, no. 3, pp. 3822–3834, Jun. 2021.

[14] Y. Jing, X. Dan, J. Yu, K. Fu, and S. M. Sharkh, "Simultaneous wireless power and multi-channel data transmission based on OFDM," *IEEE Trans. Power Electron.*, vol. 39, no. 7, pp. 8894–8903, Jul. 2024.

[15] Y. Yao, P. Sun, X. Liu, Y. Wang, and D. Xu, "Simultaneous wireless power and data transfer: A comprehensive review," *IEEE Trans. Power Electron.*, vol. 37, no. 3, pp. 3650–3667, Mar. 2022.

[16] I. Casaucao, A. Triviño, F. Corti, and A. Reatti, "SS and LCC–LCC in simultaneous wireless power and data transfer: A comparative analysis for SAE J2954-compliant EVs," *IEEE Trans. Ind. Inform.*, vol. 20, no. 6, pp. 8195–8206, Jun. 2024.
[17] Y. Fan, Y. Sun, P. Deng, H. Hu, C. Jiang, and Y. Feng, "A simultaneous wireless power and high-rate data transfer system based on transient responses regulation," *IEEE Trans. Power Electron.*, vol. 38, no. 8, pp. 9362–9366, Aug. 2023.
[18] P. Wang, Y. Sun, Y. Feng, T. Feng, Y. Fan, and X. Li, "An improvement of SNR for simultaneous wireless power and data transfer system with full-duplex communication mode," *IEEE Trans. Power Electron.*, vol. 37, no. 2, pp. 2413–2424, Feb. 2022.
[19] X. Li, F. Zheng, H. Wang, Y. Sun, X. Dai, and J. Hu, "A simultaneous power and data transfer method for dynamic wireless charging electric vehicles," *IEEE J. Emerg. Sel. Topics Power Electron.*, vol. 12, no. 1, pp. 328–340, Feb. 2024.
[20] J. Feng, G. Wei, F. Chen, J. Zhang, and C. Zhu, "Component-splitting and multisegment compensation methods for common-mode and differential-mode EMI suppression in high-power SWPDT systems," *IEEE Trans. Power Electron.*, vol. 39, no. 5, pp. 4991–4995, May 2024.
[21] T. Li, Z. Sun, Y. Wang, J. Mai, and D. Xu, "Simultaneous wireless power and data transfer system with full-duplex MIMO communication channels for underwater applications," *IEEE Trans. Ind. Inform.*, vol. 20, no. 4, pp. 6382–6393, Apr. 2024.
[22] T. Li, Z. Sun, Y. Wang, J. Mai, and D. Xu, "Undersea simultaneous wireless power and data transfer system with extended communication distance and high rate," *IEEE Trans. Power Electron.*, vol. 39, no. 3, pp. 2917–2921, Mar. 2024.
[23] C. Da, F. Li, L. Wang, C. Tao, S. Li, and M. Nie, "Analysis and implementation of underwater single capacitive coupled simultaneous wireless power and bidirectional data transfer system," *IEEE Trans. Ind. Electron.*, vol. 71, no. 12, pp. 15674–15684, Dec. 2024.
[24] L. J. Zou, Q. Zhu, C. W. Van Neste, and A. P. Hu, "Modeling single-wire capacitive power transfer system with strong coupling to ground," *IEEE J. Emerg. Sel. Topics Power Electron.*, vol. 9, no. 2, pp. 2295–2302, Apr. 2021.
[25] F. Lu, H. Zhang, and C. Mi, "A two-plate capacitive wireless power transfer system for electric vehicle charging applications," *IEEE Trans. Power Electron.*, vol. 33, no. 2, pp. 964–969, Feb. 2018.
[26] Z. Liu, Y. Su, H. Hu, Z. Deng, and R. Deng, "Research on transfer mechanism and power improvement technology of the SCC-WPT system," *IEEE Trans. Power Electron.*, vol. 38, no. 1, pp. 1324–1335, Jan. 2023.
[27] X. Gao, H. Zhou, W. Hu, Q. Deng, G.-P. Liu, and J. Lai, "Capacitive power transfer through virtual self-capacitance route," *IET Power Electron.*, vol. 11, no. 6, pp. 1110–1118, 2018.

Chaolai Da received the B.S. degree in electrical engineering and its automation from Hebei University of Technology, Tianjin, China, in 2021. He is currently working toward the Ph.D. degree in electrical engineering with the Institute of Electrical Engineering, Chinese Academy of Sciences, Beijing, China.

His research interests include undersea wireless power transfer and simultaneous wireless power and data transfer.

Fang Li received the Ph.D. degree in electrical engineering from the Institute of Electrical Engineering, Chinese Academy of Sciences, Beijing, China, in 2009.

She is currently a Professor with the Key Laboratory of Power Electronics and Electric Drives, Chinese Academy of Sciences. Her research interests include wireless power transmission, simultaneous wireless information and power transfer, and intelligent vehicle control.

Ming Nie received the B.S. degree in electrical engineering and its automation from Chongqing University of Technology, Chongqing, China, in 2021. He is currently working toward the M.S. degree in electrical engineering with the Institute of Electrical Engineering, Chinese Academy of Sciences, Beijing, China.

His research interests include undersea wireless power transfer and capacitive power transfer.

Shufan Li received the Ph.D. degree in electrical engineering from the Institute of Electrical Engineering, Chinese Academy of Sciences, Beijing, China, in 2020.

He is currently an Associate Professor with the Key Laboratory of Power Electronics and Electric Drives, Chinese Academy of Sciences. His research interests include analysis, designing, and controlling of static/dynamic wireless power transfer system.

Chengxuan Tao (Member, IEEE) received the M.S. degree in control science and engineering from Chongqing University, Chongqing, China, in 2012, and the Ph.D. degree in mechanical engineering from Beijing Institute of Technology, Beijing, China, in 2024.

He is currently a Senior Engineer with the Key Laboratory of Power Electronics and Electric Drives, Chinese Academy of Sciences. His research interests include circuit topology, analysis, and control of wireless power transfer system, especially its applications in special fields.

Lifang Wang (Member, IEEE) received the Ph.D. degree in automotive engineering from Jilin University, Jilin, China, in 1997.

She was with the Institute of Electrical Engineering, Chinese Academy of Sciences (IEECAS), Beijing, China. During the Chinese tenth-five year plan (2001–2005), she was a member of the national specialist group of Key Special Electric Vehicle Project of the National 863 Program, and she was the Head of the 863 Special EV Project Office. She is currently the Director with the Department of Vehicle Energy System and Control Technology, IEECAS. She is also the Vice Director of the Key Laboratory of Power Electronics and Electric Drives, Chinese Academy of Sciences. Her research interests include wireless charging system for EV, EV control system, EV battery management system, electromagnetic compatibility, and smart electricity use.